Electronic Supplementary Information

for

Pt-functionalized Fe_2O_3 Photoanodes for Solar Water Splitting: the Role of Hematite Nano-organization and Platinum Redox State

M. E. A. Warwick,[a] D. Barreca,[b] E. Bontempi,[c] G. Carraro,[a] A. Gasparotto,*[a] C. Maccato,[a] K. Kaunisto,[ad] T.-P. Ruoko,[d] H. Lemmetyinen,[d] C. Sada,[e] Y. Gönüllü,[f] and S. Mathur[f]

[a] *Department of Chemistry, Padova University and INSTM, 35131 Padova, Italy*. * Corresponding author E-mail: alberto.gasparotto@unipd.it

[b] *CNR-IENI and INSTM, Department of Chemistry, Padova University, 35131 Padova, Italy*

[c] *Chemistry for Technologies Laboratory, Brescia University, 25123 Brescia, Italy*

[d] *Department of Chemistry and Bioengineering, Tampere University of Technology, 33101 Tampere, Finland*

[e] *Department of Physics and Astronomy, Padova University, 35131 Padova, Italy*

[f] *Department of Chemistry, Chair of Inorganic and Materials Chemistry, Cologne University, 50939 Cologne, Germany*

EXPERIMENTAL DETAILS

Synthesis. Fe_2O_3 deposits were fabricated by means of a custom-built PE-CVD apparatus equipped with a radio frequency (RF, ν = 13.56 MHz) generator.[1] The diameter of each electrode was 9 cm and the inter-electrode distance was fixed at 6 cm. Growth experiments were performed from Ar/O_2 plasmas for a total duration of 1 h, using a fixed RF-power of 10 W and a total pressure of 1.0 mbar. The iron precursor $Fe(hfa)_2TMEDA$ (hfa = 1,1,1,5,5,5-hexafluoro-2,4-pentanedionate; TMEDA = *N*,*N*,*N*′,*N*′-tetramethylethylenediamine), synthesized according to a previously reported procedure,[2,3] was placed in an external vessel heated by an oil bath maintained at 65 °C and transported into the reaction chamber by means of electronic grade Ar (flow rate = 60 sccm). The temperature of precursor feeding lines was maintained at 140 °C in order to prevent detrimental condensation phenomena. Two further auxiliary gas-lines were used to introduce Ar (flow rate = 15 sccm) and electronic grade O_2 (flow rate = 20 sccm) directly into the reactor chamber. Basing on previous results,[4] Fe_2O_3 growth was performed at 300 °C on FTO-coated glass slides (Aldrich, 735167-1EA, ≈7 Ω/sq; lateral dimensions = 2.0 cm × 1.0 cm; FTO thickness ≈600 nm), mounted on the grounded electrode. Prior to deposition, the substrates were suitably cleaned by iterative dipping in acetone, sulphonic detergent, distilled water, and finally dried under an air flow.

Platinum sputtering on iron oxide samples was carried out in the same reactor used for PE-CVD experiments, using electronic grade Ar as plasma source. A platinum target (0.3 mm thick; Alfa Aesar®, 99%) was fixed on the RF electrode, and FTO-supported α-Fe_2O_3 matrices were mounted on the grounded electrode. Sputtering processes were performed under the following conditions: substrate temperature = 60 °C; RF-power = 5 W; total pressure = 0.3 mbar; Ar flow rate = 10 sccm. After optimization of the processing parameters, two different sputtering times

(30 and 50 min) were used to vary the overall platinum amount in the resulting composites.

Samples were *ex-situ* annealed in air for 1 h using a Carbolite HST 12/200 tubular oven prior and/or after sputtering (see Table 1) at a fixed temperature of 650 °C. The use of more severe annealing conditions was discarded to avoid the thermal degradation of the substrate.

Characterization. 2D X-ray microdiffraction (XRD^2) measurements were run in reflection mode on a Dymax-RAPID X-ray microdiffractometer equipped with a cylindrical imaging plate detector, enabling data collection from 0 to 160° (2θ) horizontally and from –45 to +45° (2θ) vertically upon using CuKα radiation. Conventional XRD patterns were then obtained by integration of 2D images.

X-ray photoelectron spectroscopy (XPS) measurements were performed on a Perkin-Elmer Φ 5600ci spectrometer using a standard AlKα radiation (1486.6 eV), at a working pressure lower than 10^{-8} mbar. The reported binding energies (BEs, standard deviation = ± 0.2 eV) were corrected for charging by assigning to the adventitious C1s signal a BE of 284.8 eV.[5,6] The analysis involved Shirley-type background subtraction and, whenever necessary, spectral deconvolution by non-linear least-squares curve fitting. In particular, the fit of the Pt4f region was done using an asymmetric line shape function through the XPS PEAK software,[7] with a constant spin-orbit coupling of 3.3 eV and an intensity ratio between the $Pt4f_{7/2}$ and $Pt4f_{5/2}$ components of 1.33.[8] Atomic percentages (at.%) were calculated by peak integration using standard PHI V5.4A sensitivity factors.

Field emission-scanning electron microscopy (FE-SEM) micrographs were collected with a Zeiss SUPRA 40 VP instrument, operating at an acceleration voltage between 5.0 and 20.0 kV, equipped with an Oxford INCA x-sight X-ray detector for energy dispersive X-ray spectroscopy (EDXS) analyses. ImageJ® software[9] was used to estimate the mean size of Pt-containing

particles, averaging over 100 independent measurements for each sample.

Atomic force microscopy (AFM) analyses were carried out using a NT-MDT SPM Solver P47H-PRO instrument operating in tapping mode in air. Root-Mean-Square (RMS) roughness values were obtained from 2×2 μm^2 images after a plane fitting procedure.

Secondary ion mass spectrometry (SIMS) analyses were carried out by means of a IMS 4f mass spectrometer (Cameca) using a 14.5 keV Cs^+ primary beam (intensity = 25 nA, stability = 0.2%) and by negative secondary ion detection, adopting an electron gun for charge compensation. Rastering was performed over a 175×175 μm^2 area, whereas secondary ions were collected from a subregion close to 8×8 μm^2 to avoid crater effects. Signals were detected in beam blanking mode (*i.e.* interrupting the sputtering process during magnet stabilization periods), in order to improve the in-depth resolution, and under high mass resolution configuration, to avoid mass interference artifacts.

Optical absorption spectra were recorded in transmission mode at normal incidence by means of a Cary 50 spectrometer, subtracting the substrate contribution. Optical band-gap energies (E_G) were evaluated by applying the Tauc formula:[2,10,11]

$$(\alpha h\nu)^n = A\,(h\nu - E_G) \quad (1)$$

where hν is the incident photon energy, A is a constant and n is an exponent dependent on the nature of electronic transitions (n = 2 for direct transitions, reported to be the strongest ones for *hematite*-based systems).[12,13] α is the absorption coefficient calculated from the Lambert-Beer law:[1,14,15]

$$\alpha = -[\ln(T)]/d \quad (2)$$

with d being the mean nanodeposit thickness calculated from cross-sectional FE-SEM analyses, and T is the transmittance after background subtraction.

Photoelectrochemical (PEC) measurements were performed at 22 °C in un-buffered NaOH solutions (pH = 13.7), using a saturated calomel electrode (SCE) as a reference, a Pt wire as counter-electrode and the Pt/Fe_2O_3 nanodeposits as working electrodes. All experiments were carried out under ambient conditions. A copper wire was soldered on the uncovered portion of the FTO substrate to establish an electrical connection, and an epoxy resin was used to seal all the exposed FTO portions, except for the working area of the electrodes.[16] The electrolyte was purged with gaseous nitrogen before each experiment in order to prevent any possible reaction with dissolved oxygen.[17-19] Linear sweep voltammetry (10 mV/s) was carried out in a potential range from -1 to 1 V *vs.* SCE using a potentiostat (PAR, Versa state IV), both in the dark and under front side illumination, using a Xe lamp (150 W, Oriel) with an AM 1.5 filter. Potentials with respect to the reversible hydrogen electrode (RHE) scale were calculated using the Nernst equation:[19-23]

$$E_{RHE} = E_{SCE} + E°_{SCE} + 0.059\ pH \quad (3)$$

where E_{SCE} is a measured electrode potential *vs*. the used reference electrode and $E°_{SCE}$ is the reference electrode standard potential *vs*. the normal hydrogen electrode.

Transient absorption spectroscopy (TAS) measurements were performed on samples with a geometric area of 3×3 cm^2 in a complete PEC cell (PECC-2, Zahner-elektrik). A standard three-electrode configuration was used having a Pt counter-electrode, an Ag/AgCl (3 M KCl) reference electrode and a 0.1 M NaOH electrolyte (degassed with N_2 prior to experiments). A potential value of 1.6 V *vs*. RHE, set by a standard potentiostat (F02A, Faraday MP), was selected to study the charge dynamics at the SCLJ, since it provided an optimal signal-to-noise ratio.

The ps transient absorption spectra were measured by using a pump-probe setup consisting of Libra F-1K (Coherent Inc.) generator producing 100 fs pulses at 800 nm (1 mJ) with a repetition

rate of 1 kHz. An optical amplifier (Topas-C, Light Conversion Ltd.) was used to provide pump pulses at the selected excitation wavelength of 355 nm (band gap excitation). The measuring component was ExciPro (CDP Inc.) equipped with two array photodetectors coupled with a spectrometer (CDP2022i) set for probe detection in the wavelength range 500 – 700 nm with averaging over 10000 excitation shots. A white light continuum, generated in a sapphire plate, was used as the probe. The maximum time range available for probing was ≈ 6 ns. The ultra-fast TAS instrumentation was described in detail elsewhere.[24]

The TAS analyses in a ms timescale were performed by using modified flash-photolysis equipment (LFP-111, Luzchem) with a photodetector (2051, New Focus) and a halogen lamp (9 W, Thorlabs SLS201/M) probe.[4] The excitation was fixed at 355 nm, with an energy density of 0.4 mJ cm^{-2}. The ms transient absorption traces were averaged 30–80 times depending on the probe intensity and detector sensitivity.

S1. Morphological characterization by Field Emission-Scanning Electron Microscopy (FE-SEM) and Atomic Force Microscopy (AFM)

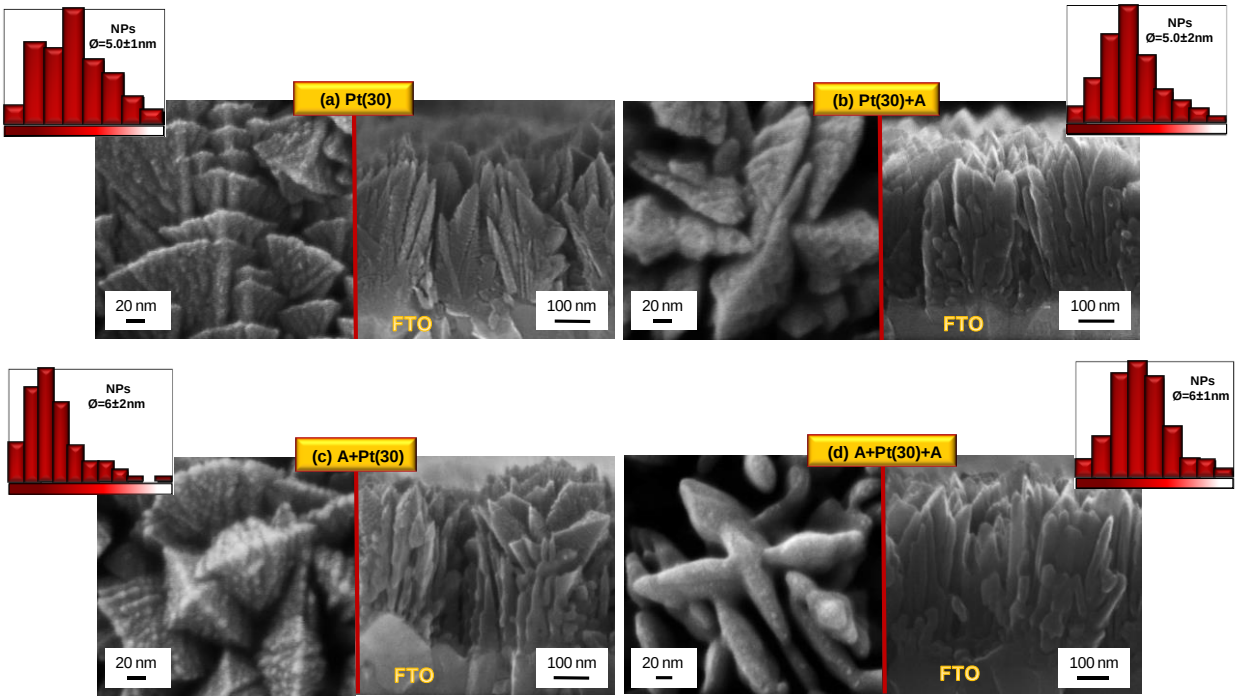

Fig. S1 Plane-view (left) and cross-sectional (right) FE-SEM images of as-prepared and annealed Pt/α-Fe_2O_3 nanosystems obtained with a Pt sputtering time of 30 min. In each case, the histogram of Pt particle size is also reported. Sample labeling as in Table 1.

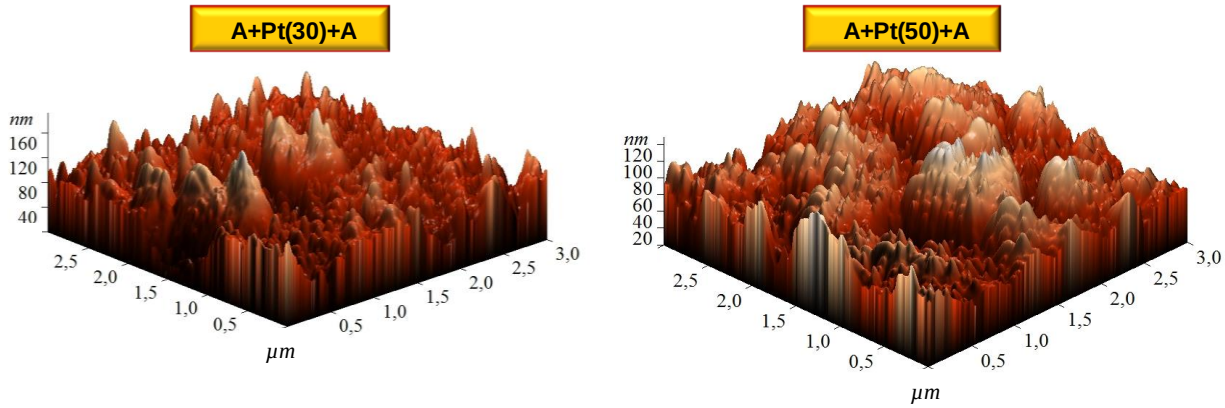

Fig. S2 Representative AFM micrographs for selected Pt/α-Fe_2O_3 specimens. Sample labeling as in Table 1. RMS values are very close to 20 nm for all the investigated specimens.

S2. H_2 plasma treatment

Following previous works,[22,25] the best performing Pt/Fe_2O_3 nanostructures were subjected to *ex-situ* hydrogen plasma processing [**A+Pt(50)+A, A+Pt(30)+A**; Table S1], in an attempt to further amplify the system photoresponses.[26] Such kind of post-growth hydrogenation treatments have already been adopted to tailor material properties through the introduction of impurity levels in metal oxide semiconductors, resulting in O-deficient systems[27,28] with an absorption extending from the UV to the IR region of the electromagnetic spectrum.[29] The exposure of the target materials to non-equilibrium plasmas offers unique chances to alter optical and electrical characteristics without inducing any pronounced morphological and mechanical alteration.[22,30] In the present case, basing on the data discussed in the main text, the reduction of oxidized Pt species to metallic platinum is expected, in principle, to further enhance the material PEC performances.

Ex-situ hydrogen plasma treatments were carried out in a PE-CVD reaction chamber for 60 min maintaining the specimens at a temperature of 300 °C, operating at a RF-power of 20 W, using electronic grade H_2 (flow rate = 200 sccm).[22,25] After the treatment, the sample color changed from brown-red to black (Figure S3).

Sample name	**Pre-annealing**	**Pt puttering time (min)**	**Post-annealing**	**H_2 plasma treatment temperature (°C)**
A+Pt(30)+A+H	650 °C	30	650 °C	300 °C
A+Pt(50)+A+H		50		

Table S1. Processing conditions for selected Pt/α-Fe_2O_3 samples subjected to *ex-situ* H_2 plasma treatments.

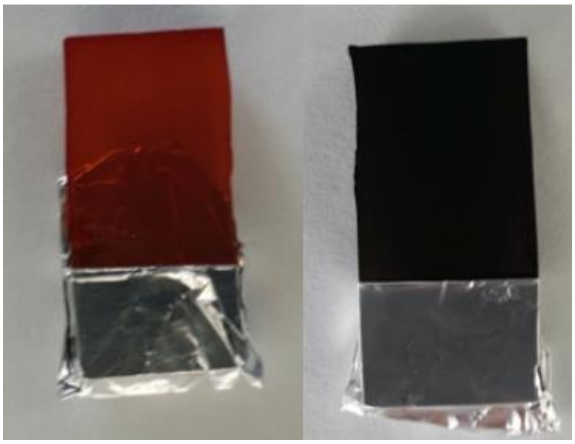

Fig. S3 Digital photographs of **A+Pt(50)+A** (left) and **A+Pt(50)+A+H** (right) samples.

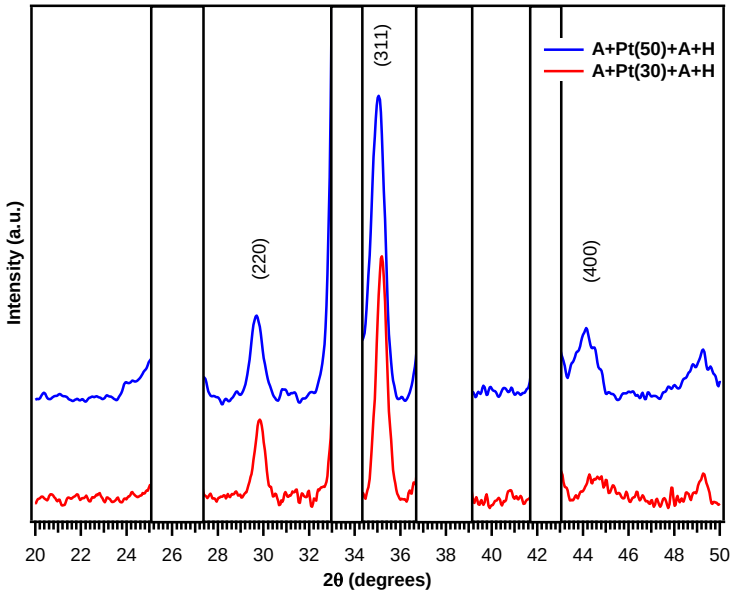

Fig. S4 XRD patterns of selected Pt/Fe_2O_3 specimens subjected to H_2 plasma treatment. Sample labeling as in Table S1.

In the case of Fe_2O_3-based materials subjected to H_2 plasma treatments, a partial reduction of the iron(III) oxide matrix to Fe_3O_4 has been reported, resulting in mixed Fe_3O_4/α-Fe_2O_3 systems with an increased content of O vacancies and H impurities incorporated in iron oxide lattice, with a substantial photoefficiency tuning.[22] Conversely, XRD analyses on the present systems subjected to hydrogen plasma treatments under the same experimental conditions (Figure S4) revealed a

complete reduction of Fe_2O_3 to Fe_3O_4 (*magnetite*). Similarly to the results regarding the pristine materials (compare Figure 1), no diffraction peaks related to platinum-containing species could be observed. In line with these observations, XPS analyses on treated materials suggest the formation of Fe_3O_4, as evidenced by the slight shift of the Fe2p component to lower BEs (Figure S5(a) and (c)).[5,18] Correspondingly, the analysis of the Pt4f peak revealed appreciable modifications, related to the progressive reduction to Pt(0) species, which appeared to be the dominant ones (Figure S5(b) and (d); see also the main paper text).

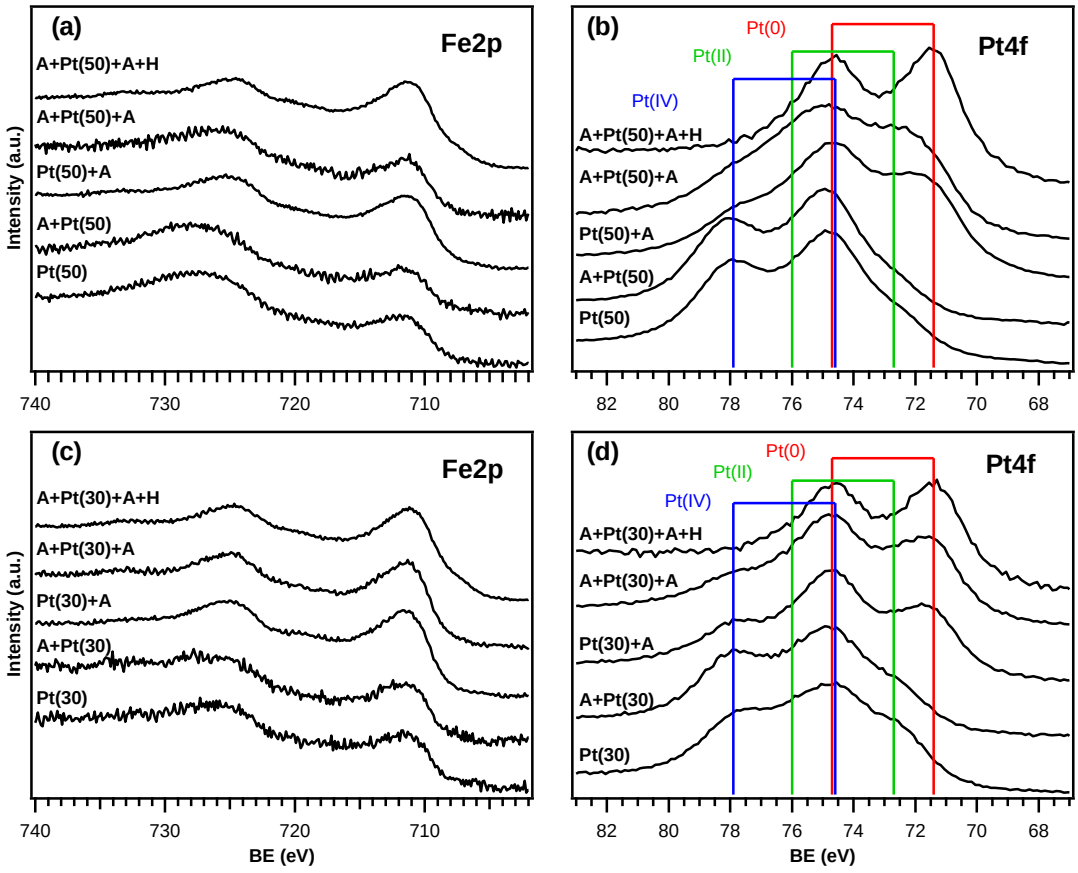

Fig. S5 XPS spectra for Fe2p and Pt4f regions for Pt/α-Fe_2O_3 specimens obtained with a Pt sputtering time of 50 min (a,b) and 30 min (c,d). Colored lines mark the positions for Pt(0), Pt(II) and Pt(IV) signals. For sample labeling, refer to Tables 1 and S1.

Basing on the data discussed in the main text, the increased content of metallic platinum might be considered favorable for an eventual improvement of the material PEC responses, but, at variance with previous studies on PE-CVD Fe_2O_3 photoanodes,[22] the treated nanosystems showed a significant photoactivity degradation.

This phenomenon, that might appear surprising, can be traced back to the fact that the ultimate effect of hydrogen plasma treatment results from the delicate counterbalance of various fundamental processes, *i.e.* charge carrier generation, charge transportation and charge collection.[25] In the present case, the performance degradation of Pt/Fe_3O_4 systems obtained after plasma treatment with respect to the pristine Pt/α-Fe_2O_3 ones can be due to a concurrence of different causes. It is worthwhile highlighting that Fe_3O_4, a semimetallic oxide with a narrow band gap (0.1-0.4 eV), can ease the recombination of photogenerated charge carriers, explaining thus the significant lowering of PEC performances after hydrogen plasma treatments.[28] In addition, the latter can likely induce in the target systems the formation of an excess of defects, acting as hole traps.[25] A comparison of the actual results with literature ones highlights that *ex-situ* hydrogen plasma processing should be carried out under conditions that avoid a complete α-$Fe_2O_3 \rightarrow Fe_3O_4$ reduction and to produce an optimal defect concentration, since overcoming a certain threshold results in performance degradation. A complete understanding of the mechanisms associated with hydrogen treatment, which goes beyond the simple H introduction in the system lattice, with a partial reduction and the formation of oxygen vacancies, requires further detailed studies under different experimental conditions.[22] To this regard, additional experiments as a function of H_2 plasma treatment temperature and duration are currently under way.

S3. Transient absorption spectroscopy

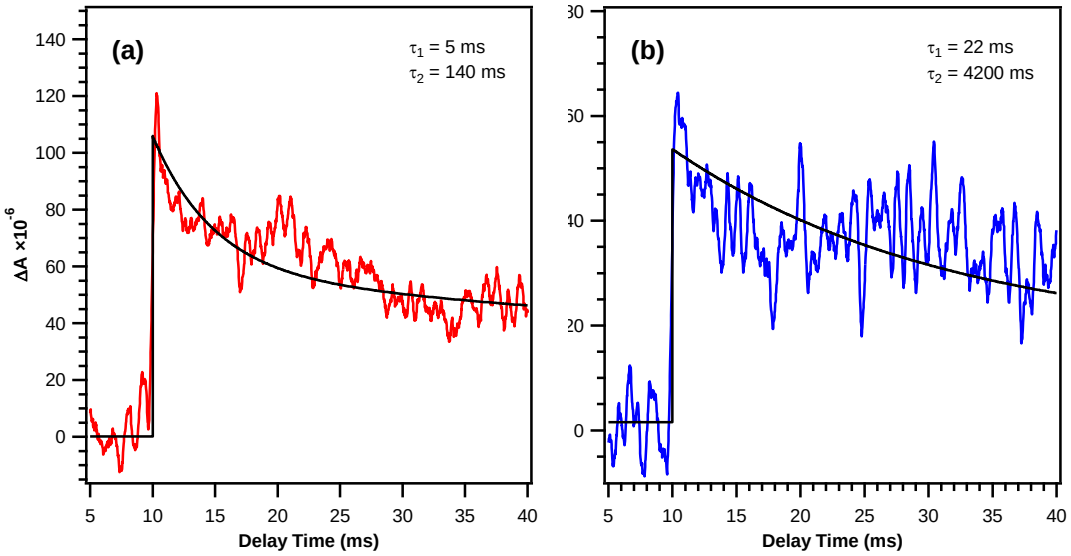

Fig. S6. Transient absorption decays of specimens **Pt(50)** (a) and **A+Pt(50)+A** (b) in a ms timescale at a probing wavelength of 650 nm. The decays are smoothed by using the Savitzky-Golay method with 50 smoothing point. The solid lines represent bi-exponential fits of the raw data.

References

1. D. Barreca, G. Carraro, A. Gasparotto, C. Maccato, C. Sada, A. P. Singh, S. Mathur, A. Mettenbörger, E. Bontempi and L. E. Depero, *Int. J. Hydrogen Energy*, 2013, **38**, 14189-14199.
2. G. Carraro, D. Barreca, E. Comini, A. Gasparotto, C. Maccato, C. Sada and G. Sberveglieri, *CrystEngComm*, 2012, **14**, 6469-6476.
3. D. Barreca, G. Carraro, A. Gasparotto, C. Maccato, R. Seraglia and G. Tabacchi, *Inorg. Chim. Acta*, 2012, **380**, 161-166.
4. M. E. A. Warwick, K. Kaunisto, D. Barreca, G. Carraro, A. Gasparotto, C. Maccato, E. Bontempi, C. Sada, T.-P. Ruoko, S. Turner and G. Van Tendeloo, *ACS Appl. Mater. Interfaces*, 2015, submitted.
5. J. F. Moulder, W. F. Stickle, P. E. Sobol and K. D. Bomben, *Handbook of X-ray Photoelectron Spectroscopy*, Perkin Elmer Corperation, Eden Prairie, MN, USA, 1992.
6. D. Briggs and M. P. Seah, *Practical Surface Analysis: Auger and X-ray Photoelectron Spectroscopy*, John Wiley & Sons: New York, 2nd ed., 1990.
7. F. Le Formal, S. R. Pendlebury, M. Cornuz, S. D. Tilley, M. Grätzel and J. R. Durrant, *J. Am. Chem. Soc.*, 2014, **136**, 2564-2574.
8. L. K. Ono, B. Yuan, H. Heinrich and B. Roldan Cuenya, *J. Phys. Chem. C*, 2010, **114**, 22119-22133.
9. S. R. Pendlebury, A. J. Cowan, M. Barroso, K. Sivula, J. Ye, M. Grätzel, D. R. Klug, J. Tang and J. R. Durrant, *Energy Environ. Sci.*, 2012, **5**, 6304-6312.
10. A. P. Singh, A. Mettenbörger, P. Golus and S. Mathur, *Int. J. Hydrogen Energy*, 2012, **37**, 13983-13988.

11. Y.-P. Hsu, S.-W. Lee, J.-K. Chang, C.-J. Tseng, K.-R. Lee and C.-H. Wang, *Int. J. Electrochem. Sci.*, 2013, **8**, 11615-11623.

12. K. Sivula, R. Zaboril, F. L. Formal, R. Robert, A. Weidenkaff, J. Tucek, J. Frydrych and M. Grätzel, *J. Am. Chem. Soc.*, 2010, **132**, 7436-7444.

13. N. Mirbagheri, D. Wang, C. Peng, J. Wang, Q. Huang, C. Fan and E. E. Ferapontova, *ACS Catal.*, 2014, **4**, 2006-2015.

14. I. Cesar, K. Sivula, A. Kay, R. Zboril and M. Grätzel, *J. Phys. Chem. C*, 2009, **113**, 772-782.

15. N. T. Hahn, H. Ye, D. W. Flaherty, A. J. Bard and C. B. Mullins, *ACS Nano*, 2010, **4**, 1977-1986.

16. S. Kumari, A. P. Singh, Sonal, D. Deva, R. Shrivastav, S. Dass and V. R. Satsangi, *Int. J. Hydrogen Energy*, 2010, **35**, 3985-3990.

17. G. Rahman and O.-S. Joo, *Mater. Chem. Phys.*, 2013, **140**, 316-322.

18. Y.-S. Hu, A. Kleiman-Shwarsctein, A. J. Forman, D. Haxen, J.-N. Park and E. W. McFarland, *Chem. Mater.*, 2008, **20**, 3803-3805.

19. S. Shen, M. Li, L. Guo, J. Jiang and S. S. Mao, *J. Coll. Interface Sci.*, 2014, **427**, 20-24.

20. O. Zandi, J. A. Beardslee and T. Hamann, *J. Phys. Chem. C*, 2014, **118**, 16494-16503.

21. L. Steier, I. Herraiz-Cardona, S. Gimenez, F. Fabregat-Santiago, J. Bisquert, S. D. Tilley and M. Grätzel, *Adv. Funct. Mater.*, 2014, **24**, 7681–7688.

22. A. Mettenbörger, T. Singh, A. P. Singh, T. T. Järvi, M. Moseler, M. Valldor and S. Mathur, *Int. J. Hydrogen Energy*, 2014, **39**, 4828-4835.

23. S. Shen, J. Jiang, P. Guo, C. X. Kronawitter, S. S. Mao and L. Guo, *Nano Energy*, 2012, **1**, 732-741.

24. D. Sirbu, C. Turta, A. C. Benniston, F. Abou-Chahine, H. Lemmetyinen, N. V. Tkachenko, C. Wood and E. Gibson, *RSC Adv.*, 2014, **4**, 22733-22742.

25. A. Sasinska, T. Singh, S. Wang, S. Mathur and R. Kraehnert, *J. Vac. Sci. Technol. A*, 2015, **33**, 01A152.

26. Y. Ling, G. Wang, D. A. Wheeler, J. Z. Zhang and Y. Li, *Nano Lett.*, 2011, **11**, 2119-2125.

27. G. Wang, Y. Ling, H. Wang, X. Yang, C. Wang, J. Z. Zhang and Y. Li, *Energy Environ. Sci.*, 2012, **5**, 6180-6187.

28. S. K. Mohapatra, S. E. John, S. Banerjee and M. Misra, *Chem. Mater.*, 2009, **21**, 3048-3055.

29. X. Chen, L. Liu, P. Y. Yu and S. S. Mao, *Science*, 2011, **331**, 746-750.

30. J. Pan, R. Ganesan, H. Shen and S. Mathur, *J. Phys. Chem. C*, 2010, **114**, 8245-8250.